Check for updates

Bridging nano- and microscale X-ray tomography for battery research by leveraging artificial intelligence

Jonathan Scharf[1 ✉], Mehdi Chouchane[2,3], Donal P. Finegan [4], Bingyu Lu[1], Christopher Redquest[5], Min-cheol Kim[1], Weiliang Yao[6], Alejandro A. Franco[2,3,7,8], Dan Gostovic[9], Zhao Liu[9], Mark Riccio[9], František Zelenka[9], Jean-Marie Doux [1 ✉] and Ying Shirley Meng [1,10 ✉]

X-ray computed tomography (CT) is a non-destructive imaging technique in which contrast originates from the materials' absorption coefficient. The recent development of laboratory nanoscale CT (nano-CT) systems has pushed the spatial resolution for battery material imaging to voxel sizes of 50 nm, a limit previously achievable only with synchrotron facilities. Given the non-destructive nature of CT, in situ and operando studies have emerged as powerful methods to quantify morphological parameters, such as tortuosity factor, porosity, surface area and volume expansion, during battery operation or cycling. Combined with artificial intelligence and machine learning analysis techniques, nano-CT has enabled the development of predictive models to analyse the impact of the electrode microstructure on cell performances or the influence of material heterogeneities on electrochemical responses. In this Review, we discuss the role of X-ray CT and nano-CT experimentation in the battery field, discuss the incorporation of artificial intelligence and machine learning analyses and provide a perspective on how the combination of multiscale CT imaging techniques can expand the development of predictive multiscale battery behavioural models.

X-ray computed tomography (CT) is well known in the medical and scientific research communities as a non-destructive imaging technique in which contrast originates from the materials' absorption coefficients[1]. The attenuated X-ray beam due to the sample interaction is collected, converted and reconstructed with sophisticated algorithms to produce cross-sectional and three-dimensional (3D) images[2–6]. The resultant data provide valuable non-invasive information about a sample's morphology and internal structure. In the medical field, CT has led to countless discoveries and treatments that have greatly impacted the health of populations[7]. In the past two decades, the impact of CT has expanded outside the medical field to general metrology[8,9], and has considerably impacted the development of battery systems and other electrochemical devices[2,10,11].

With CT technology rapidly improving, commercial lab-based systems are now able to achieve similar resolutions to those of high brilliance synchrotron beamlines. However, with the increasing resolutions and applications of CT in electrochemical fields, more complex datasets are being explored, which motivates the need for advanced analysis techniques to fully harness detailed insights about samples. This has led to the recent leveraging of artificial intelligence (AI) and machine learning (ML) to assist in the segmentation and analysis of complex datasets, or to act as a bridge between experimental data and multiphysics and/or multiscale modelling[12–14]. As such, AI and ML have proved to be valuable tools

to substantially reduce the time necessary to process large CT datasets while precisely labelling features of interest.

In this Review, we explore the larger outlook of X-ray CT in the battery field and discuss how AI and ML can impact data analysis and computational modelling. In the first section, we discuss the key technological developments that have made X-ray CT an advanced tool suitable for battery characterization. In the second section, we outline the virtues and limitations of CT for a variety of battery chemistries as well as the key morphological parameters that can be extracted from the experiments. The third section covers the methods of the appropriate data analysis and filtering to extract these parameters and discusses the emerging uses of AI and ML in battery modelling. Finally, in the last section we explore the perspective of the future of X-ray CT, in which AI and ML can be used in combination with other techniques to fully characterize battery systems and develop multiphysics and multiscale predictive models.

Development of X-ray CT

X-ray CT was first used in 1971, when Sir Godfrey Hounsfield performed the first patient brain CT scan[15–17]. Since then, CT has evolved from a technique primarily used in the medical community to a tool widely used across multiple disciplines in the scientific and engineering world[2,18]. To track the development of CT, Fig. 1 showcases the year of publication versus the reported voxel size for works in the medical and electrochemical storage fields[19–21]. Here, a voxel

[1]Department of Nano-Engineering, University of California San Diego, La Jolla, CA, USA. [2]Laboratoire de Réactivité et Chimie des Solides (LRCS), Université de Picardie Jules Verne, UMR CNRS 7314, Hub de l'Energie, Amiens, France. [3]Réseau sur le Stockage Electrochimique de l'Energie (RS2E), FR CNRS 3459, Hub de l'Energie, Amiens, France. [4]National Renewable Energy Laboratory, Golden, CO, USA. [5]Department of Chemical Engineering, University of California San Diego, La Jolla, CA, USA. [6]Department of Materials Science and Engineering, University of California San Diego, La Jolla, CA, USA. [7]Alistore-ERI European Research Institute, FR CNRS 3104, Hub de l'Energie, Amiens, France. [8]Institut Universitaire de France, Paris, France. [9]Thermo Fisher Scientific, Waltham, MA, USA. [10]Sustainable Power and Energy Center (SPEC), University of California San Diego, La Jolla, CA, USA. ✉e-mail: scharfjd@gmail.com; jdoux@eng.ucsd.edu; shmeng@ucsd.edu
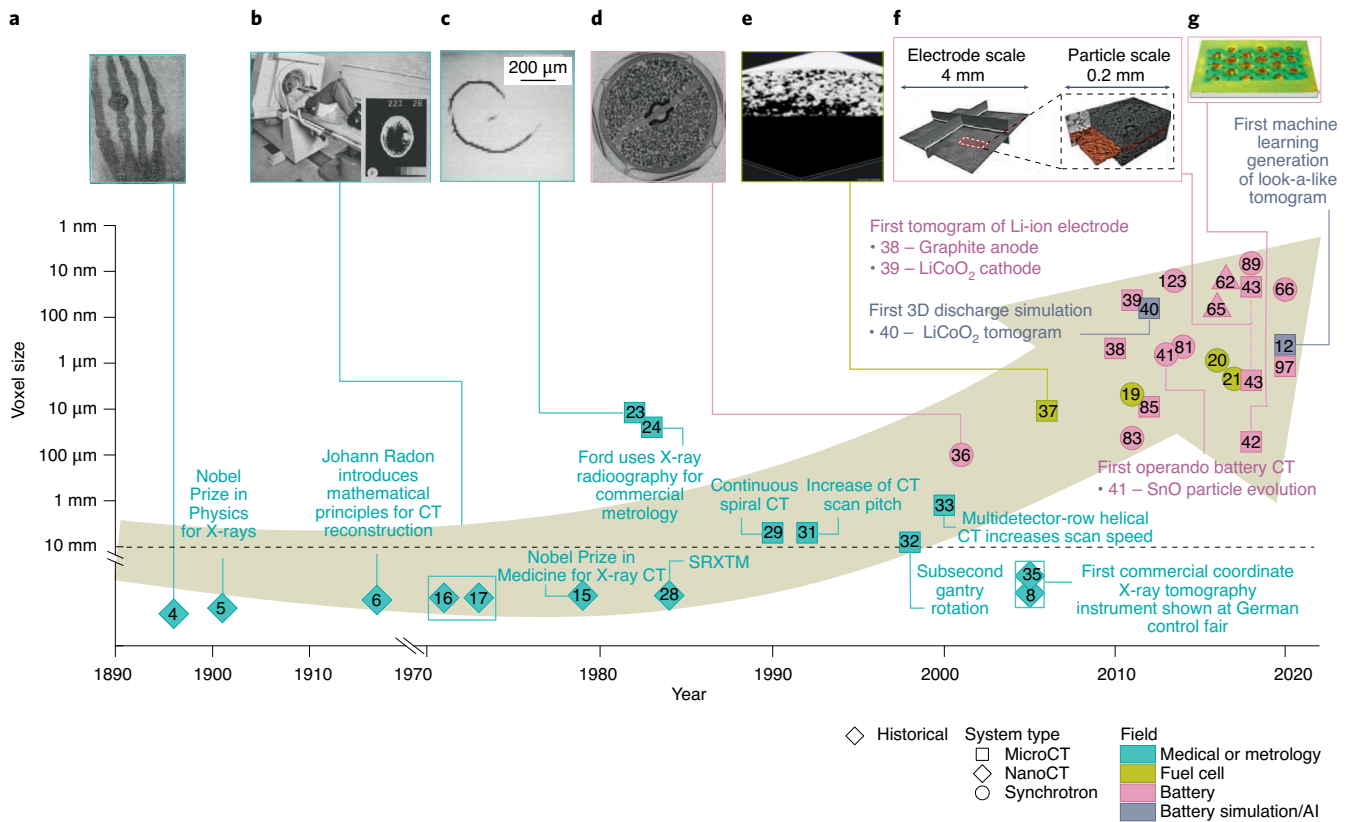
Fig. 1 | History and trends of CT. Notable advancements in X-ray CT showing the trend of decreasing tomogram voxel size with time. **a–f**, Discovery of X-rays (Wilhelm C. Röntgen) (**a**), beginning of CT (Godfrey Hounsfield) (**b**), first tomogram of a tropical freshwater snail (**c**), first tomogram of a battery of a Na-Ni/NiCl zebra cell (**d**), early fuel cell CT of water distribution in a gas diffusion layer (**e**), multiscale imaging of a silicon anode battery (**f**) and investigation of failure in a Samsung Galaxy Note 7 (**g**). Colours represent the various fields that works are related to: blue, medical; green, fuel cell; pink, battery; purple, battery simulation. Symbols indicate historical advancements (diamonds) and works that pertain to micro-CT (squares), synchrotron (circles) and nano-CT (triangles) systems. Symbols below the dotted line show notable CT-related events or works for which voxel sizes are not reported. Reference numbers are given on the symbols. Panels reproduced with permission from: **a**, ref. [4], AAAS; **c**, ref. [23], Wiley; **d**, ref. [36], IOP; **g**, ref. [42] under a Creative Commons licence (https://creativecommons.org/licenses/by/4.0/). Panels adapted with permission from: **b**, ref. [17], British Institute of Radiology; **e**, ref. [37], IOP; **f**, ref. [43], Elsevier.

is a 3D representation of a 2D pixel and corresponds to the smallest cube of information obtained from a scan. The spatial resolution is often thought of as at least two to three times the voxel size, but can be larger due to blurring and imaging artefacts that impede the distinction of fine features.

In the early 1980s, CT started to gain traction outside the medical field in the broader scientific and industry community, and in 1982, the first microtomogram was taken of a freshwater snail with a 12 μm voxel size[22,23]. In 1983, Ford reported the first industry application of an in-house built microscale CT (micro-CT) system in which they distinguished features with a spatial resolution of 25 μm (refs. [18,24]). In the same year, Grodzins and co-workers[25–27] proposed the theoretical principles to utilize synchrotron-sourced radiation to provide enhanced contrast and resolution for CT, and in 1984, Thomson et al.[28] reported the first synchrotron radiation X-ray tomographic microscopy (SRXTM) measurement. Meanwhile, through the late 1980s to 1990s, developments in the biomedical community progressed laboratory-scale CT from a slow step-and-shoot approach[7] to that of continuous gantry rotation[7,29–32] with multidetector rows[33,34], which drastically decreased the acquisition speed for larger areas.

CT deployment in electrochemical device characterization
CT systems used in metrology benefited greatly from the improvements in speed and detection developed by medical CT. However,

it was not until 2005 that a CT machine was dedicated to metrology and industrial applications were introduced[8,35]; the first microtomograms of a battery[2,36] and fuel cell[10,37] were reported in 2001 and 2006, respectively. As shown in Fig. 1, numerous CT works in the electrochemical field began to emerge shortly after the commercialization of this tool. In the early 2010s, the first tomograms of a Li-ion battery positive and negative electrodes were reported, which illustrated the capability to distinguish the active material ($LiCoO_2$) from an inactive phase[38,39]. The first 3D discharge simulation based on tomography images quickly followed in 2012[40].

Further development allowed for novel and more creative studies to be performed: in 2013, Ebner et al. performed the first operando battery CT experiment to visualize and quantify the electrochemical and mechanical evolution of SnO particles in a Li-ion battery electrode[2,41]. In 2018, Loveridge et al. used X-ray CT to identify the failure mechanism in the Galaxy Note 7, which were recalled due to battery explosions[42]. The reconstructed tomograms in this work revealed defects in the positive tab welding area that resulted in electrical shorts, which led to a thermal runaway. This example illustrates the usefulness of CT and the incentive of the recent efforts towards multiscale imaging by the electrochemical community[43]. Finally, an increasing number of works are now leveraging AI and ML, for instance, to imitate in silico electrode tomograms similar to those in experimental CT[12].

Table 1 | Common tomography techniques in materials science

Technique	Resolution	FOV	Destructive or non-destructive	Vacuum level	Information extracted
X-ray CT[55,76–79,158]	~10 nm	~100 µm	Non-destructive	Not required	Porosity, surface area, tortuosity, chemical composition
Cryogenic electron tomography[159]	~1 nm	~100 nm	Destructive	~10^{-8} kPa	3D nanostructures
FIB[160]	~10 nm	~10 µm	Destructive	~10^{-6} kPa	Porosity, surface area
Atom probe tomography[161]	~1 Å	~100 nm	Destructive	~10^{-11} kPa	Atomic arrangements
NMR imaging[162]	~1 mm	~10 cm	Non-destructive	Not required	3D tomography
Time-of-flight secondary ion mass spectrometry[163]	~10 nm	~10 µm	Destructive	~10^{-8} kPa	Chemical composition

Capabilities of lab-based and synchrotron sources

For research in materials science, both lab-based and synchrotron facilities have made great advancements over the past decade. In 2014, Maire and Withers wrote a review[44] on quantitative X-ray tomography in which they outlined how X-ray CT data were no longer only used for qualitative insights but also increasingly for the quantitative analysis of material properties. This transition from qualitative to quantitative has only accelerated since 2014, as imaging capabilities facilitated greater spatial and temporal resolutions. Lab-based X-ray CT systems now routinely achieve resolutions of 1 µm or less, with specialized systems able to achieve resolutions as low as tens of nanometres[45]. This multilength scale capability for lab-based systems allows for the ex situ imaging of structural properties from tens of nanometres to millimetres[45,46].

Recently, laboratory CT systems enabled dual or tri-energy imaging via multiple quasi-monochromatic beam energies[47]. Software packages were developed to extract the best detail from images taken at the different energies. For example, images taken with lower energies may have an enhanced resolution and sharpness for materials that consist of low-atomic-mass elements. This software framework can also be utilized for correlative workflows between different microscopy methods. The strengths of individual techniques are leveraged in combined datasets that provide a heighted resolution or larger sample sizes. The temporal resolution of laboratory sources has also shown tremendous progress over the past decade, but remains insufficient for many operando and in situ analyses of structural dynamics in the range of minutes to hours. This limitation in temporal resolution is largely due to the challenge of thermal management at the anode source in lab-based X-ray systems that limits the flux of X-rays. Some progress has recently been made to increase the flux of lab-based systems by improving heat dissipation, such as liquid metal jet anodes as demonstrated by Excillum AB or composite anodes with high thermal conductivity materials, such as diamond, as demonstrated by Sigray. Synchrotron sources avoid this challenge by not having metal targets, but instead use magnetic fields to change the momentum of electrons and produce X-rays as the electrons are accelerated around a polygonal 'ring'. Synchrotron sources are also rapidly evolving, with major synchrotrons, such as the National Synchrotron Light Source II, Advanced Photon Source and the European Synchrotron Radiation Facility having completed or planned upgrades for increased photon flux density and coherence for faster imaging and greater sensitivity[48,49]. For example, the European Synchrotron Radiation Facility's Extremely Brilliant Source is expected to present 100 times its previous brilliance and coherence, and so facilitate new opportunities for high-energy and high-spatial and -temporal-resolution imaging[50]. Although an updated review of the temporal and spatial resolution capabilities of international synchrotrons is beyond the scope of this Review, synchrotron sources now achieve tomograms

with voxel sizes of 20–50 nm in under 30 minutes[51,52] and such times may not be limited by the flux available, but by other factors such limitations of scintillators, optics or detectors. It is also important to note that X-ray nanoscale CT (nano-CT) has different requirements to those of micro-CT. Although micro-CT systems generally involve X-rays that travel directly from the source through the sample to the detector (absorption CT), nano-CT techniques generally involve additional optics for focusing or phase contrast. Examples of the optics needed for nano-CT and phase contrast are explained in other publications[53,54]. Lab-based nano-CT systems can also achieve resolutions of around 50 nm, in particular the Zeiss Ultra 810 and the Sigray TriLambda systems, which are leading this field. Although several public research facilities around the world house these lab-based systems, few specialize in battery research, notably groups at Carnegie Mellon University, University College London and the National Renewable Energy Laboratory. This evolution of both laboratory- and synchrotron-based capabilities has continued to present new opportunities to understand the highly dynamic behaviour of electrochemical energy devices. For consistency, in the following we refer to 3D tomographic data collected at synchrotron facilities by scanning transmission X-ray microscopy or by transmission X-ray tomography as SRXTM[51,52].

X-ray CT in the battery field

Although several tools are already routinely used to characterize the morphology of electrochemical devices or materials, X-ray CT presents considerable advantages that the other techniques do not possess. For instance, focused ion beam (FIB)–scanning electron microscopy (SEM), transmission electron microscopy (TEM) and secondary ion mass spectrometry all require a vacuum, which makes in situ and operando studies difficult if not impossible for most battery systems. Moreover, these 3D reconstruction techniques are destructive and require invasive sample preparation methods, and accurate segmentation of the reconstruction data can be particularly challenging as material can be observed through the sample's porosity, which makes it difficult to identify exactly the extent of the pores of the sample. In comparison, X-ray CT is non-destructive and does not require a vacuum for high-resolution imaging, so it is ideal to evaluate 3D morphological changes in situ or operando in practical battery systems. CT can also be used to distinguish and segment species based on the varying X-ray absorption, which thus allows for select materials to be studied dynamically. A comparison of the X-ray CT with common battery characterization techniques is given in Table 1.

Although X-ray CT has many benefits over other tomography techniques, the relatively limited resolution and lack of chemical information for most lab-scale CT systems make it challenging to study electrode interfaces, a crucial aspect of battery systems. Nevertheless, CT is still a relatively new tool for the electrochemical

Box 1 | CT species segmentation and workflow

In battery electrodes, the three main phases typically observed in an X-ray CT scan are the active material, binder and pores. A proper segmentation of these is mandatory to ensure the quality of the extracted battery-specific parameters (such as particle size, porosity and tortuosity). As the contrast in X-ray CT is dictated by the material's X-ray absorption coefficient, the simplest segmentation method is thresholding, which differentiates materials based on the numerical grey value distribution[164,165]. With global thresholding, the segmentation is performed on the grey-value histogram of an entire 3D dataset. As can be seen in Fig. 3c–e, filtering is a critical step, as it can reveal three distinct grey-value regions in a Li-ion cathode (corresponding to binder, porosity and active material), which were indistinguishable before filtering.

Manual segmentation and global thresholding are, nevertheless, subject to human error and bias, and therefore a variety of automatic segmentation methods were developed[164,165]. In contrast to global thresholding, adaptive local segmentation methods account for neighbourhood statistics to separate the phases in an image. Among the multiple local segmentation methods, Bayesian Markov random field segmentation, watershed segmentation and converging active contours were shown to be the most efficient

for multiclass segmentation, with trade-offs specific to each method and sample[164]. ML algorithms, such as the Trainable Weka Segmentation plugin for ImageJ[166], are also employed to increase the reliability of segmentation. These algorithms utilize training sets to adaptively recognize phases with an improved accuracy and are increasingly employed in X-ray CT segmentation in the electrochemical community[100,167].

Above all, the limiting factor in segmentation is data quality, and it is crucial to have a workflow in which the dataset is optimally acquired and properly filtered to adequately define phases. The workflow can be separated into three stages: (1) preprocessing (artefact removal, filtering and sharpening), (2) segmentation (global and local thresholding) and (3) postprocessing (denoising). Denoising algorithms are often used to prepare the dataset for structural analysis. As each stage is interconnected, filters should be chosen with the segmentation method in mind. Moreover, care must be taken as overfiltering can be an issue as well: the mean filter can introduce 'unrealistic' values, and filters such as erosion, dilation and delineation can skew multiclass data[164,168]. Therefore, knowledge of the various filters and segmentation methods is needed to ensure a proper extraction of the crucial morphological parameters.

field, and as high-resolution nano-CT systems are increasingly developed and used, it will become a common battery characterization tool as high-resolution 3D imaging with a precise species segmentation is now possible.

Materials CT parameters. To understand the usefulness of CT in battery research, it is important to know the information and morphological parameters that it can provide. Reconstructed volumes can showcase large-scale device architecture, such as that by Yin et al., who demonstrated a uniform electrode contact when flexing a printed Zn–AgO battery[55]. However, apart from large-scale architecture, many morphological parameters can also be extracted, which provide powerful insights into the electrode structure and performance. These morphological parameters can come in a variety of types: surface area, volume, particle size distribution or porosity and pore networks; pore networks refer to networks of interconnected pores that can be quantified by observables, as described later in this section.

Surface area and volume information are commonly used in battery research to analyse electrodes and are the most intuitive to observe and quantify from reconstructed volumes. However, owing to the limited resolution of the traditionally used micro-CT systems, it is more common to approximate the surface area as quantification is limited to the scan resolution. Surface area measurements can evaluate electrode wettability, whereas volumetric analysis can determine the thickness variation and volume expansion during battery operation. In an initial operando battery CT study, Ebner et al. evaluated the volume expansion of a SnO electrode as it was lithiated[41]. During reduction, the repeated measurements using SRXTM revealed a 250% volume expansion due to lithiation that was only partially recovered during oxidation. The thickness and the spatial distribution of the solid–electrolyte interface was also quantified, which showed its increase with lithiation. CT volume extraction has also proved particularly useful for silicon anode batteries[56–58] in the evaluation of volume expansion during lithiation (up to 280% for $Li_{15}Si_4$) (ref. [59]), which is one of the main limitations that hinders cycle lifetimes. In a 2019 study, in situ SRXTM was used to track the expansion and contraction dynamics of Si electrodes during

electrochemical cycling[59]. The thickness variation and changes in the delaminated area were studied, and the microsized crack volume fraction was quantified to reveal the failure mechanism in non-maturated electrodes.

Particle analysis can also be performed using CT: through segmentation (Box 1), particles can be separated and their individual volumes can be analysed to provide valuable information about their size and distribution. This type of analysis can be especially useful for in situ or operando studies, in which the morphological evolution of active material particles can be tracked and analysed dynamically. For instance, Gent et al. studied the heterogeneity of lithiation in secondary particles in causing accelerated capacity fade[60]. Additionally, Zernike phase contrast[61] is a technique often used in nano-CT because it uses phase differences in the transmitted X-ray signal to differentiate materials, and thus is employed to segment out the three phases (for example, active material, binder and pore) typically observed in Li-ion battery electrodes[62,63]. With a high spatial resolution of 50 nm, Komini Babu et al. characterized the particle contact area variation with additives to illustrate their influence on the electrode contact resistance[62]. This can be particularly valuable in quality assurance to study the influence of manufacturing and synthesis conditions on particle morphology. For instance, Heenan et al. showed how five-minute-long scans with a nano-CT system were sufficient to fully resolve cathode particles and directly quantify the variation in the particle's asymmetry, sphericity and local surface roughness[64]. This study also quantified the internal voids within individual particles, which should be minimized to maximize volumetric energy density.

Similarly, pores and void spaces in battery electrodes can be visualized and quantified with CT. For instance, Frisco et al. performed the first investigation of the solid–electrolyte interface build up with nano-CT and quantitatively extracted the pore distributions in commercial Li-ion cells to reveal a collapse of the anode pore structure during cycling[65]. They showed a decrease of more than half the pore volume with cycling, and qualitatively demonstrated, using 3D tomograms, the solid–electrolyte interface build up, which results in an increased cell impedance[65]. Similarly, Su et al. used operando SRXTM to perform the first characterization of $Li–O_2$ battery cathodes with 3D tomography and extracted the pore distribution using
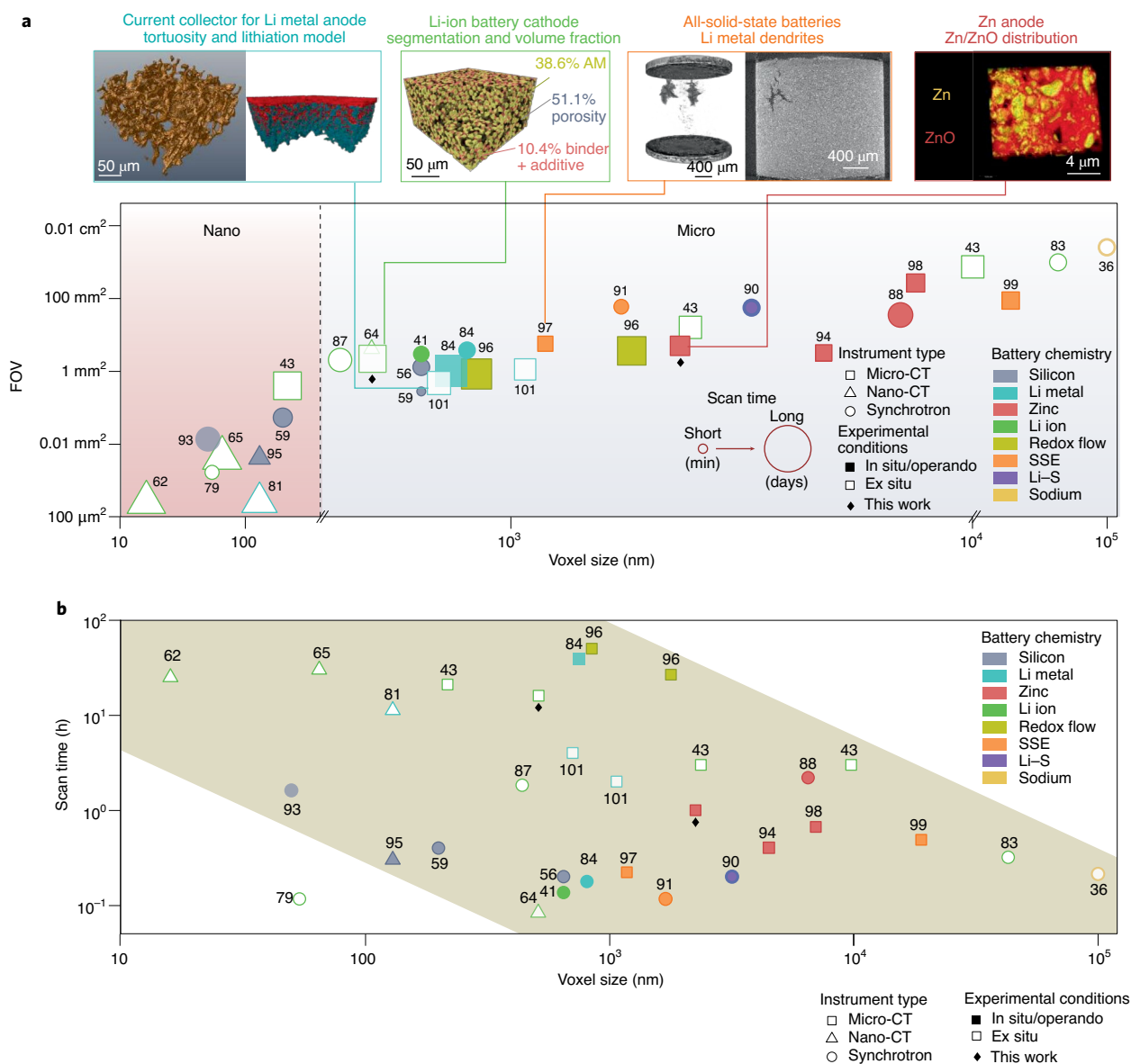
Fig. 2 | Experimental trends of CT in the battery field. a,b, Trends of FOV (**a**) and scan time (**b**) with voxel size for various battery chemistries, CT systems and experimental conditions. In **a**, the symbol area reflects the CT scan time indicated in **b**. Reference numbers are given above the symbols. In the green inset of **a**, AM refers to the active material particles in the electrode. The markers indicated with the diamond symbol and 'this work' refer to original experimental data showcased in Fig. 3 for Li-ion and zinc anode battery chemistries. SSE refers to work related to solid-state electrolyte batteries. Left blue inset of **a** adapted with permission from ref. [101], American Chemical Society.

an interconnected pore model for the scanned Li_2O_2 electrode[66]. By using Zernike phase contrast, they were able to image and distinguish the void spaces from the lighter species, such as carbon and Li_2O_2 discharge products, and successfully extract nanosized pores on the order of 100 nm.

Once segmented, an interconnected pore network model can be extracted and utilized to study the mesostructure evolution during fabrication processes, such as calendering[67]. For instance, Torayev et al. introduced a 3D-resolved pore network model extracted from a CT image of a $Li-O_2$ battery carbon electrode[68]. The extracted pore network consists of a family of spheres with different sizes connected by cylindrical throats and describes species transport through the electrode. Thanks to models such as this, researchers have shown that electrode samples that have the same average porosity and tortuosity factor but different pore interconnections can result in differing discharge performances[69,70].

Finally, CT can also allow us to measure the tortuosity or tortuosity factor (square of the tortuosity), which can quantify how tortuous an electrode is by analysing the connection of pores within a structure. The tortuosity factor was first introduced by Epstein in 1989[71], and can be defined for electrochemical systems by the porosity multiplied by the ratio of bulk diffusion to the effective diffusion due to the tortuous path, as shown in equation (1):

$$k = \tau^2 = \epsilon \frac{D_{bulk}}{D_{eff}} \tag{1}$$

where k is the tortuosity factor, τ is the tortuosity, ϵ is the porosity, D_{eff} is the effective diffusion coefficient and D_{bulk} a bulk diffusion coefficient[71,72]. Tortuosity in CT has gained considerable attention in the past decade[12,73,74] and is especially impactful for understanding the transport of electrolyte ions through battery electrodes.
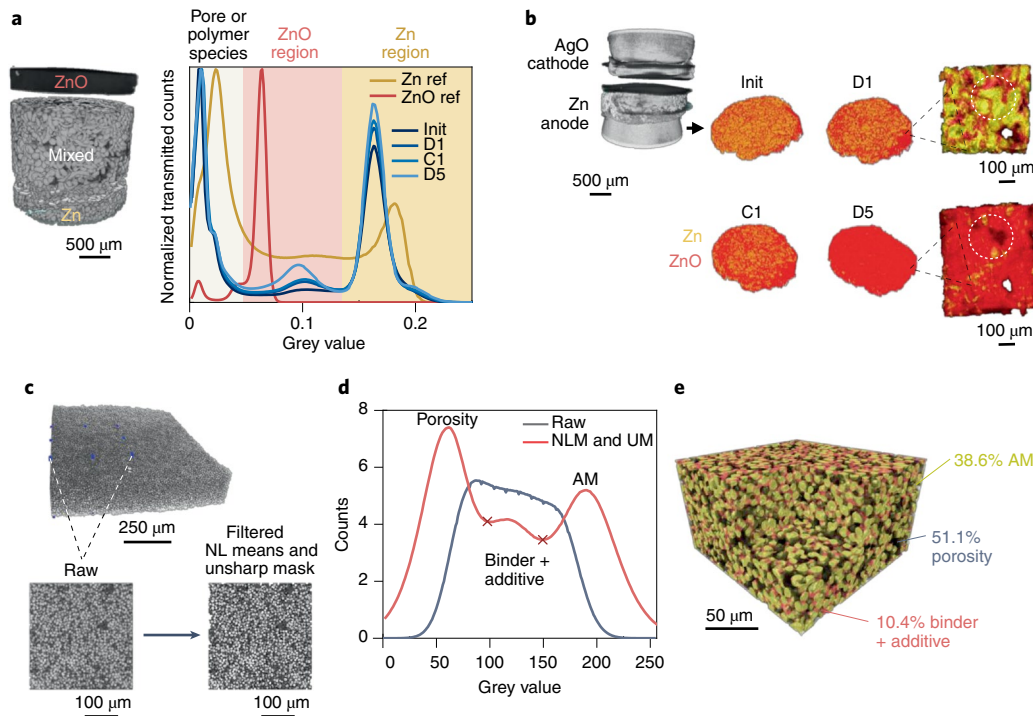
Fig. 3 | CT segmentation and analysis of battery systems. a,b, Aqueous zinc batteries. **b–e,** Li-ion batteries. **a,** Volume rendering and grey value histograms of Zn and ZnO references (ref) and the anode region of a cycled battery. **b,** Volume renderings of a battery full cell and anode at different states of charge. Init, initial; D1, first discharge; C1, first charge; D5, fifth discharge. **c,** Cropped $LiNi_{0.5}Mn_{1.5}O_4$ cathode and *x–y* slices before and after non-local means (NL or NLM) and unsharp mask (UM) filtering. **d,** Histogram of raw data and after applying filters. X indicates threshold regions implemented in the watershed-based segmentation. **e,** Segmented filtered tomogram and volume fraction of the three phases.

For instance, Ebner et al. used SRXTM to study the tortuosity anisotropy of three common Li-ion electrodes with varying porosities to represent various particles shapes (spherical, triaxial ellipsoidal and platelet)[75]. They showed that an increased geometric tortuosity factor in the plane perpendicular to the current collection can impact the achievable Li-ion battery power density and cycling performance and predicted a factor of four improvement in the battery discharge rate with platelet-shaped particles in graphite electrodes[75].

Experimental trends in battery X-ray CT. Since the first battery microtomogram in 2001[2,36], CT has developed into a versatile technique in which various CT system types offer different benefits. Laboratory-scale micro-CT is the most common CT system used in metrology and battery research, due to its large field of view (FOV) (~130 cm² in the *x–z* direction for large scans), ease of access and use, and relatively high spatial resolution of up to ~500 nm (refs. [3,76,77]). However, even with submicrometre resolution, micro-CT systems fall short in studying nanoscale phenomena. For this reason, battery researchers turned to SRXTM, with spatial resolutions reported in battery studies that reach as low as 50 nm (refs. [78,79]). The main compromises are the beamline time cost, increased sample preparation complexity and limited FOV. To circumvent this, laboratory-scale nano-CT offers spatial resolutions of up to 50 nm (ref. [80]), rivalling SRXTM without the necessity for high brilliance synchrotron radiation.

Figure 2a shows the trend in FOV, voxel size and scan duration for CT experiments in battery literature[81–94]. As many CT studies do not report the spatial resolution, the FOV was plotted versus the voxel size, as the voxel size scales with and is typically slightly less than half the spatial resolution. As shown, regardless of the battery chemistry, there is a general trend in which the FOV decreases with smaller voxel sizes and is dependent on the CT

system used. Indeed, in the nanoregime, synchrotron and nano-CT dominate use, whereas in the microregime, micro-CT systems are implemented more often. Additionally, in the nanoregime, nano-CT experiments are mostly ex situ due to the long scan time, and synchrotron experiments are mainly in situ or operando, which illustrates the difficulty in performing dynamic experiments at a limited FOV and long scan times (Fig. 2b). However, operando experimentation with lab-scale nano-CT was demonstrated using a quasi-4D approach, in which slower 3D scans were intermittently recorded between extended high temporal resolution radiography sequences[95].

In the microregime, lab-scale micro-CT dominates, and in situ or operando experiments are quite common, as such experiments tend to elucidate degradation mechanisms and key phenomena in batteries[94,96–99]. For many experiments, microsized voxels are small enough to perform novel studies for a variety of battery systems. For instance, shown in the orange inset of Fig. 2a, microsized Li-metal dendrites can be resolved in all-solid-state batteries[97]. Although X-ray CT is not able to distinguish light elements (such as metallic Li) from porosity in a denser matrix (such as the solid electrolyte), a proper sample design makes this possible by leveraging another tool, such as X-ray diffraction. Microsized particles on the scale of 10–100 μm can be easily resolved with micro-CT, such as the case for the Li-ion cathode and the zinc anode in the green and red insets, respectively. Particle-scale analysis can be performed for both chemistries (Fig. 3), and in situ studies are even possible, as is the case for the zinc anode[100]. Modelling can also be performed using the reconstructed scans as input. For instance, the blue inset of Fig. 2a shows a reconstructed porous Cu current collector scanned by micro-CT and a model of the lithiation in the structure, in which the porosity and tortuosity can be optimized to maximize the cycle life[101].
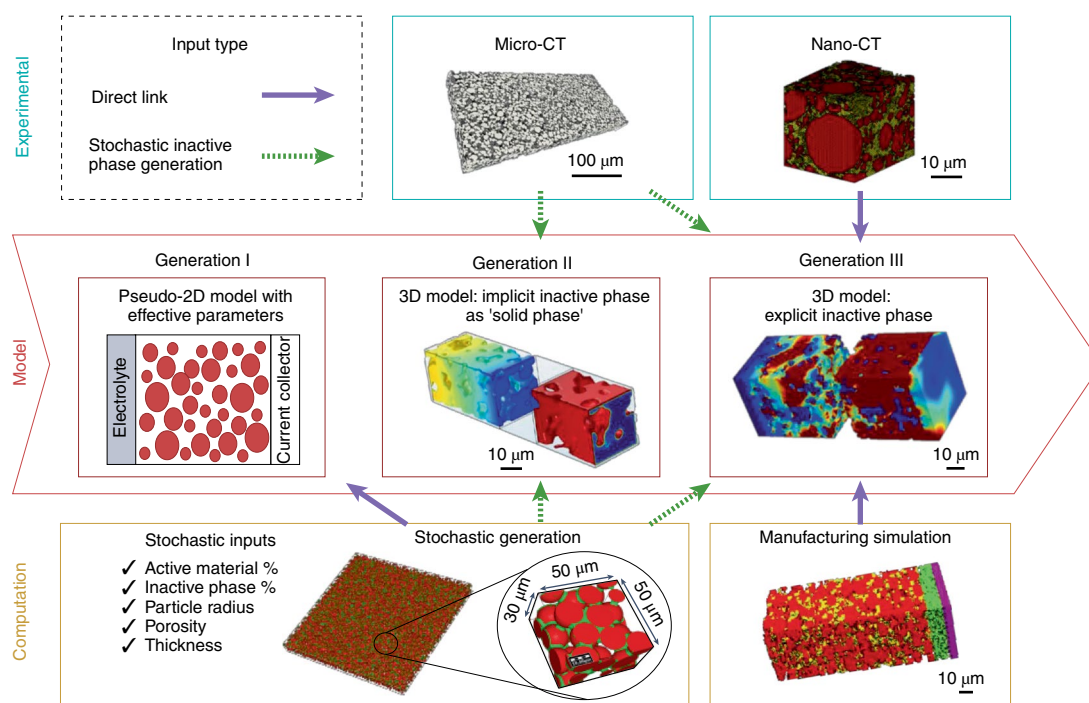
Fig. 4 | Relationship between experimental tomography data, cell model and computation of electrochemical data in battery systems. To enable 3D models of the battery, tomography data at the micro- and nanoscale can be used either directly (purple arrows) or after stochastic inactive phase generation (green arrows). This allows us to compute the electrochemical performance of the electrode to study the effect of its morphology. Credit: Mariem Maiza (LRCS) for the generation II and stochastic generation images.

The battery chemistry of interest also strongly influences the type of instrument used. For instance, as Li is a very light element that weakly interacts with X-rays, it is difficult to image and resolve when it is close to dense materials, such as solid electrolytes or cathodes using traditional micro-CT, which use higher X-ray energies of around 30–160 kV (refs. [3,76]). For this reason, the Li-ion battery studies shown with the green symbols in the microregime of Fig. 2 mainly focused on studying device structures or composite electrodes rather than investigating lithium growth. For instance, Carter et al. (43 in Fig. 2) investigated the delamination in a lithium iron phosphate battery and the porosity and diffusion-based tortuosity factor of the graphite anode structure[43]. They were able to distinguish between graphite, void and copper, but did not specifically look at Li species. Many studies to investigate Li with CT use Zernike phase contrast with nano-CT or SRXTM systems, which can use lower X-ray energies of around 5–8 keV. However, there are still constraints on the FOV and sample preparation and size for these instruments, which is why Li-ion CT studies, such as Frisco et al. (65 in Fig. 2)[65] and Ghorbani Kashkooli et al. (79 in Fig. 2)[79], tend to be ex situ. However, operando nano-CT experimentation with larger form-factor coin cells has been demonstrated[95], and custom in situ and/or operando cells can be developed to help study dynamic phenomena, as shown by Vanpeene et al. (59 in Fig. 2)[59] who used X-ray CT-compatible custom Swagelok cells to study volume expansion in situ using SRXTM with a 200 nm voxel size.

Progress and challenges in in situ and operando X-ray CT. From the onset of X-ray microtomography, it was recognized that sample preparation and the design of in situ environments would be an important challenge for decades to come[102]. Researchers frequently aim to achieve the maximum resolution and contrast for samples that are as large as possible to achieve good statistics and obtain representative volume measurements. However, maximizing the contrast and signal-to-noise ratio for a given X-ray energy and specific composition requires limiting the sample to a specific width[103]. This is due to the attenuation of X-rays through the sample thickness, and that there is an optimal extent to which the sample of interest interacts with the incoming beam. Many different materials are used within the current and next-generation Li-ion batteries, but for simplicity the example of the electrode material $LiNi_{0.8}Co_{0.1}Mn_{0.1}O_2$ (NMC811) is discussed here—attenuation coefficients for other materials can be determined from open-source databases[104]. For an X-ray energy within the range of 3–8 keV (the typical range of lab-based nano-CT systems), the optimal thickness of a NMC811 sample is between 10 μm and 100 μm (ref. [103]). Synchrotron sources can tune the X-ray energies to be monochromatic within a wide range from single-digit kiloelectronvolt to energies that approach 100 keV, and thus researchers can weigh the suitability of synchrotrons and beamlines for their specific application. As most monochromatic or quasi-monochromatic sources operate in the range of 5–30 keV, the optimal width of an NMC811 electrode is between 10 μm and 1,000 μm, which raises the challenge of designing a small enough Li-ion cell to achieve the relevant in situ or operando conditions. For many quantitative measurements of electrode microstructural properties, it is critical to achieve a representative volume element[105]. Thereafter, building an environment that facilitates operando or in situ imaging is needed. Of most interest is an electrochemical operation, but some work has focused on mechanical experiments, such as the in situ compression of electrodes to replicate calendering[106]. Ideally, all environments would be cylindrical to achieve symmetry around the axis of rotation during imaging, which would involve circular disks of electrodes with diameters between 10 μm and 1,000 μm. Specialized laser milling was recently shown to achieve diameters down to 80 μm with little effect on the electrode microstructure[106]. With these conditions in mind, operando cell environments have evolved over the past decade[107], but still suffer from design challenges that can jeopardize their performance, reliability and operational relevance. Minimizing the

Box 2 | Artefacts and filtering in CT

X-ray CT data analysis aims to obtain the truest depiction of the sample or structure analysed. However, experimental artefacts can distort the X-ray projections, which eventually leads to data misinterpretation. As such, data that contain artefacts can make segmentation challenging, and thus disallow the in-depth analysis of complex structures such as electrodes. Image noise is one of the most common artefacts[169], as well as cupping and streaks or dark bands from beam hardening[164,170,171]. As polychromatic X-rays are used in micro-CT, low-energy photons are disproportionately absorbed, and the average energy of the beam increases or hardens. This results in cupping, in which the beam is hardened more through the middle of an object than at the outer edges, and so a uniformly dense material will appear non-uniform[170,171]. Streak artefacts or dark bands occur due to differences in material absorption (that is, heavy elements next to light elements), with the beam in one area of the scan hardened more than in another area[171]. This is especially problematic for Li-ion batteries, in which light elements, such as Li, may be near heavier elements, such as Cu. Beam-hardening effects can be partly mitigated experimentally using physical filters that preharden the X-ray spectrum to remove low-energy photons[170].

Other artefacts can originate from instrument issues or improper scan parameters. Low X-ray transmission through the sample (typically below 20%) can result in artefacts, such as image noise and streaking, and is a common issue for scanning materials with high X-ray absorption coefficients. This can be resolved by tailoring the energy and acquisition time (either through the exposure time or number of back projections) to allow for more of the transmitted signal to be collected by the detector. For instance, undersampling of the projections needed to reconstruct a sample can cause artefacts known as view and ray aliasing[171], in which fine stripes appear to radiate from the edges of or close to structures. View aliasing originates from a too-large interval between projections and ray aliasing originates from undersampling within a given projection. In general, it is recommended to improve the data quality as much as possible by selecting the appropriate initial scan parameters through the image processing stage before image reconstruction.

Most artefact reduction occurs during post-processing after reconstruction, in which filtration algorithms can lessen or remove experimental artefacts and smart segmentation methods can be applied to separate out species for further analysis. Beam hardening can be treated numerically with a low-pass smoothing filter, whereby the smoothed image is used to detect large-scale intensity variations caused by beam hardening, or by a less error-prone iterative approach, which uses sequential histogram-based segmentation with a grey-value classification to lessen the effects of beam hardening[164,172,173].

Image noise is commonly addressed with a multitude of filtering algorithms[173]. Neighbourhood statistical filters consider neighbouring voxels grey values and apply a kernel operation, in which voxels values are multiplied by a set of weights and then averaged over the sum of the weights to smooth or correct for noisy data[173]. Such filters are differentiated by the type of kernel used, namely, mean, median, mode, minimum, maximum and Gaussian filters. Although filters such as these tend to blur the original data, several strategies were developed to retain particles and pore edges, such as the non-local means and anisotropic diffusion filters[164,173,174] and the unsharp mask filter used to improve image contrast[173,175,176].

---

amount of material is not of interest to imaging, but is necessary for cell integrity and operation, such as the casing or current collectors, and is challenging. Eliminating the risk of highly attenuating materials, such as current collectors blocking the FOV, is also challenging, but can sometimes be avoided by having more low attenuation but functional materials in the FOV, such as thick Li electrodes or graphite inserts in cylindrical cells[108]. Common issues include: damaging beam exposure[109], poor control of pressure applied on the cell, stagnant gas that causes poor ionic or electronic contact and exposure of cell materials to contaminants, which include air[110]. To minimize beam damage, reducing the total exposure as much as possible helps, but this can conflict with the objectives of the experiment by necessitating a reduced data collection. Another way to reduce beam damage for most materials within cells is to use high-energy beams that avoid the high photoelectric absorption around the K edge of atoms. High-energy beams tend to interact less with the sample, but are also more challenging to manipulate via the optics methods necessary for nano-CT and thus most nano-CT systems operate at energies below 12 keV. A discussion on beam damage to polymer fuel cells and the ways in which the European Synchrotron Radiation Facility enables higher energies to avoid such damage is provided by Kulkarni et al.[111]. The high impedance that is often associated with bespoke operando cell designs can limit their ability to achieve high-rate conditions, which necessitates modifications of well-proved cell designs, such as coin cells[112]. Current state-of-the-art operando cell designs for high-resolution imaging are based on plastic union fittings with steel rod current collectors that seat electrodes around 1 mm in diameter[57,113,114], but much opportunity remains to improve the reliability, rate performance and ease of assembly. When a functional operational design that is suitable for the X-ray imaging conditions is achieved, further

challenges await to minimize artefacts in reconstructions, systematic errors and data processing for quantitative analyses, such as those outlined in Boxes 1 and 2.

CT analysis, simulation and modelling

The knowledge and large quantity of information gained from X-ray CT data lead to promising outcomes in the computational modelling of batteries. The Newman's model, a first-generation mathematical model of a Li-ion battery, was developed in 1993[115,116]. It describes ionic transport in the concentrated electrolyte, lithium transport in the active material and intercalation electrochemistry at the interface between the active material and electrolyte. This model is supported on a 2D Cartesian representation of the cell, with an extra polar coordinate dimension for the active material particles (generation I models (Fig. 4)) and is therefore also referred to as pseudo-2D. As this is a 2D approach, several input parameters are necessary to consider the geometrical features of the electrodes and the cell, such as the separator thicknesses, active material particle size, active surface area (surface area of contact between the active material and electrolyte), porosity and tortuosity factor of both electrodes. Although some of these morphological parameters (for example, tortuosity factor and active surface area) are challenging to evaluate using experimental techniques[117], the stochastic generation of 3D electrode mesostructures based on the experimental parameters was shown to be a valuable method.

To stochastically generate an electrode mesostructure, several parameters are needed: electrode composition (active material/carbon/binder volume ratio), particle radius distribution and porosity and thickness of the electrode. In essence, the active material (typically as spheres) is generated randomly in the simulation box until the desired values are reached. Several observables, such

as the amount of overlap between the spheres or the surface area, can be tuned to achieve the desired configuration. Then, the inactive phase can be added by controlling its morphology, that is, as a film around the active phase or as clusters[118,119]. This approach allows access to larger electrode volumes than those experimentally achievable with nano-CT. Some commercial and academic algorithms (for example, https://www.math2market.com) are reported for electrode generation[120] and for porous media analysis to extract tortuosity factors[121]. An alternative to the extraction of the morphological parameters is the direct use of the generated 3D electrode mesostructures in electrochemical performance models. For this purpose, the inactive phase (carbon/binder) can either be merged with the active material as the solid phase (generation II models (Fig. 4))[122–126] or be explicitly considered in the 3D model (generation III models (Fig. 4))[73,118,127,128].

However, even full stochastic electrode mesostructure generation may not be sufficient to replace the real battery electrode texture. In that sense, tomography images were used in the recent years to increase the reliability of 3D battery cell computational models. Electrode mesostructures, reconstructed from micro-CT images, were used for this purpose by adding the inactive phase stochastically[128–130]. Extracting the carbon and binder additive domains from micro-CT data is, indeed, challenging due to a too coarse spatial resolution of over ~500 nm. The dataset therefore needs further work to add the binder and carbon to the active material region. The use of micro-CT images allows the models to account for realistic active material shapes and their impact on electrochemical performance[40,131]. For instance, micro-CT has been used in redox-flow battery modelling to capture a representative volume, which is usually much larger than that for Li-ion batteries[132–134]. In this context, it was used to predict the electrolyte impregnation and electrochemical response of a redox flow battery using three different electrode mesostructures that originate from micro-CT data[135]. However, this technique still has limitations, namely its inability to resolve the spatial location of the inactive phase in the case of Li-ion batteries. This ability is required to investigate the impact of the arrangement of the active and inactive phases on the electrochemical, transport and thermomechanical processes within the electrodes. For instance, the ionic transport through the electrolyte is especially impacted by the interconnectivity of pores—to extract this requires the segmentation of the active and inactive phases[68].

In nano-CT, the inactive phase can be distinguished from the active material and the porosity. The extracted structure can be directly used in the generation III models, without any additional steps. However, the high resolution comes at the cost of a narrower FOV, which results in a small volume of the imaged electrode. As a result, issues related to the representativeness of the volume have arisen and are addressed in the literature[136,137]. Additionally, such a multiphase structure can be challenging to import in a finite element–volume method model, especially for numerous interfaces between a large number of phases.

In recent years, several tools have been reported to overcome this challenge[120,138–140]. In 2019, the first generation III battery cell electrochemical model, with a positive electrode extracted from nano-CT data, was reported with an effective porosity and tortuosity for the inactive phase[141]. Furthermore, in state-of-the-art modelling, efforts have been made to limit as much as possible the use of average geometrical parameters. In 2020, several generation III model studies were reported, with resolved structures of the inactive phase and the ability to have no geometrical parameter as a model input[73,142]. This explicit representation of the structure is the key element to capture heterogeneities in the cell. For instance, for the 3D modelling of all-solid-state batteries, locating the actual positions of voids in the electrode is of the utmost importance to understand the device limitations.

Lastly, a new strategy is to achieve representative generation III models without the need for tomography data: the simulation of the electrode manufacturing process[67,125,143]. By this method, the structure, from the slurry to the final calendered electrode, can be predicted with the inactive phase considered explicitly throughout the process[144,145]. With the help of experimental inputs (slurry viscosity, porosity of the calendered electrode and so on), these models are validated at each step. Despite using some geometrical approximations, such as spherical particles, this approach yields satisfactory results and links experimental data with modelling, and thus paves the way towards predictive digital twins of an entire manufacturing processes and showcases its impact on battery performance predictions.

Future of battery X-ray CT

Correlative workflow characterization. Although X-ray CT is a powerful non-destructive imaging tool, it still suffers from several limitations, such as the inability to distinguish chemical species with similar X-ray absorption, or to provide nanoscale information about the sample's morphology. As such, one of the main strategies to overcome these shortcomings is to combine X-ray CT with other complementary imaging techniques through correlative imaging. Several studies have already shown that both low- and high-resolution X-ray CT scans can be used to determine a region of interest which is then milled using FIB–SEM. Subsequently, volume reconstruction can be performed, and the data can be aligned with the high-resolution CT scan. Moreover, FIB–SEM benefits from the multiple detectors, such as energy-dispersive X-ray spectroscopy, electron backscatter diffraction (EBSD), wavelength dispersive X-ray analysis, Raman spectroscopy and time-of-flight secondary ion mass spectrometry, which provide valuable insights by correlating chemical and morphological information. As already shown in the literature, a lamella of the region of interest can then be used for scanning transmission electron microscopy analysis, which provides nanoscale-resolution imaging, combined with crystallographic and spectroscopic information owing to electron energy loss spectroscopy and electron diffraction. This method was successfully applied in 2014 by Burnett et al. to study the corrosion of stainless steel, as EBSD and energy-dispersive X-ray spectroscopy combined allows us to determine both element segregation and grain orientation[146]. Similarly, Slater et al. were able to combine micro-CT with nano-CT and scanning transmission electron microscopy/energy-dispersive X-ray spectroscopy by using plasma FIB milling, and gain insights into the influence of grain boundary orientation in cavity formation in Type 316 stainless steel[147].

More recently, Apeleo Zubiri et al. demonstrated that coupling lab-scale nano-CT with electron tomography was an efficient way to combine the higher resolution of electron tomography with the wider FOV of nano-CT[148]. As such, the ML-assisted segmentation of the pores in zeolite particles from the CT data was improved considerably by using the segmentation of the higher-resolution electron tomography data as a training dataset.

In the battery field, a few studies were successful at applying correlated tomography to electrode composites or separators[12,52,149,150]. The combination of high-contrast absorption X-ray tomography with ptychographic X-ray CT was shown to be able to provide a detailed microstructure of Si composite anodes, in which the Si particles were distinguished from graphite and the carbon-binder domain, and was even able to resolve the solid–electrolyte interface layer[52]. The obtained dataset was then used to model the state of the charge distribution of individual Si particles. On the cathode side, FIB cross-sections were used to help segment the nano-CT data of a $LiNi_{0.33}Mn_{0.33}Co_{0.33}O_2$ electrode, which allowed the porosity network and carbon-binder domain to be resolved[149]. This information was then successfully combined with a lower-resolution micro-CT scan to evaluate the tortuosity factor of the electrode. SEM cross-section
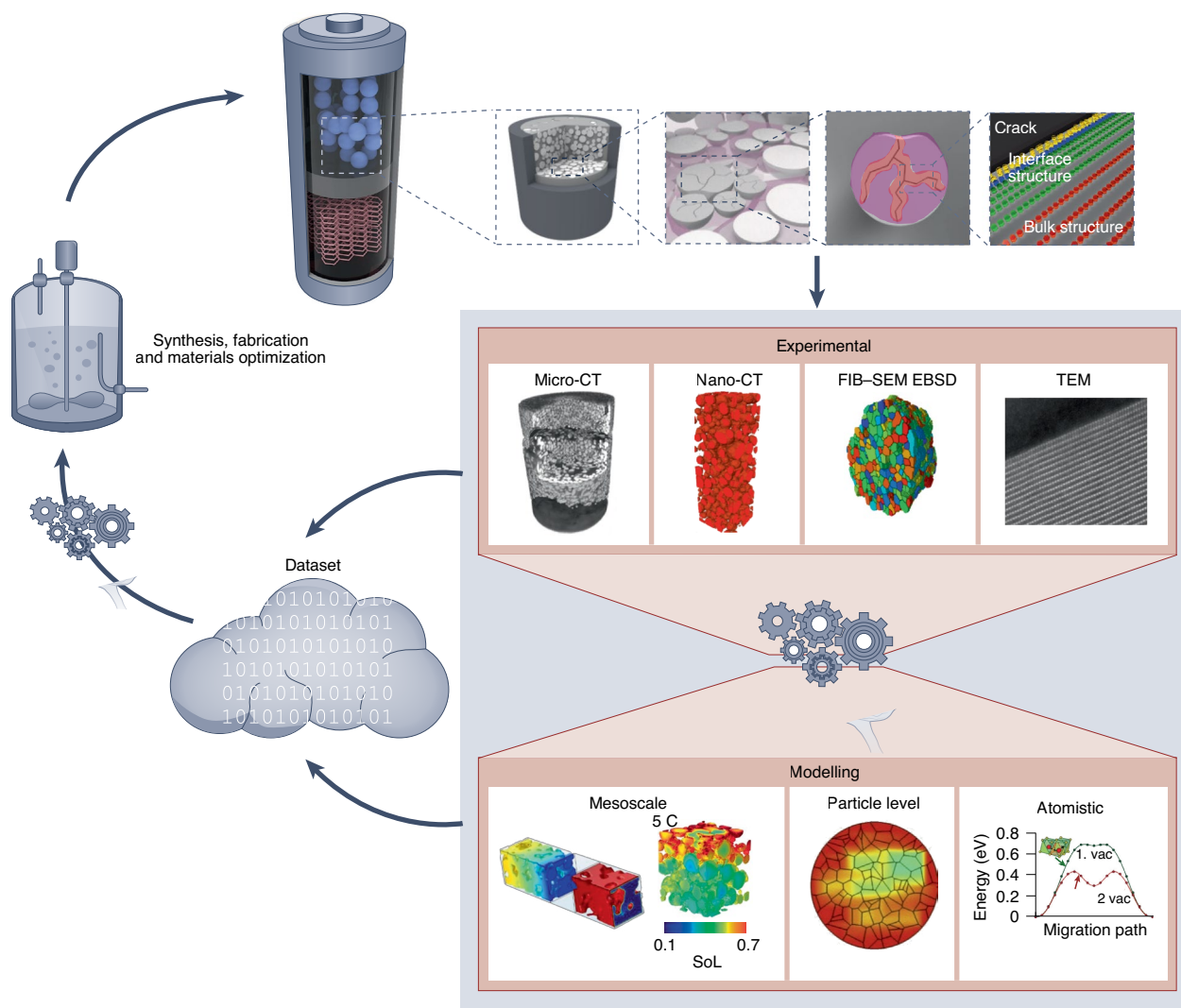
Fig. 5 | Correlative workflow analysis and modelling. Combining CT and advanced characterization techniques in the development of comprehensive predicative models. Illustrated is the connection between experimental characterization data with modelling using AI, ML and cyclical workflow to improve the synthesis, fabrication and battery performances using predictive models. SoL, state-of-lithiation; vac, vacancy. Adapted with permission from: ref. [149] (micro-CT image), ref. [73] (right mesoscale image), ref. [154] (particle-level image) and ref. [155] (atomic image) all under a Creative Commons licence (https://creativecommons.org/licenses/by/4.0/). Credit: Mariem Maiza (LRCS) for the left mesoscale image.

views were also combined with X-ray CT data of Li-ion battery separators to stochastically generate fibrils in the porous network. These fibrils, too small to be directly observed by micro-CT, were shown to have a significant influence on the prediction of the effective diffusion coefficient[150].

Correlative tomography, by employing a low-to-high-resolution approach, is a flourishing technique that can provide the multiscale information needed for the future of battery materials research. Combined with tools such as stochastic generation and electrochemical modelling, deep insights into the underlying limitations of different battery systems can be gained. Nevertheless, some technical considerations still need to be addressed before this method can be widely applied to all types of system. Principally, when working with sensitive materials, all the steps of the analysis must be carried out under a protective atmosphere, which necessitates a careful design of the samples and transfer devices. Moreover, although the possibility to investigate a region of interest with nanometre-scale resolution makes this method powerful, to reduce the size of the sample sufficiently for high-resolution tools (that is, nano-CT or even TEM) can still be a challenge, and tools with a higher milling

throughput than that of FIB, such as plasma FIB, laser plasma FIB or broad ion beam milling, are often required.

Perspective of CT data analysis with AI and ML. It is evident that the future of CT data analysis is strongly correlated with the transformative tools of the emerging digital era, which includes AI, ML and multiscale modelling. ML techniques (within the wider field of AI) present a plethora of opportunities to elucidate structure–function relationships for porous electrode images produced by CT and/ or multiphysics and/or multiscale modelling. In short, ML techniques give a computer the power to learn and self-correct from data to build 'models' (also called ML models) in an automatic way. These models can then be used to predict qualitative or quantitative outcomes, which allows us, for instance, to unravel complex parameter interdependencies in multidimensional datasets and to automatize processes that would be too time-consuming to perform manually. Regarding the latter, segmenting and distinctly labelling complex features in CT images, such as cracks[13] or regions of delamination[14], can be conducted more quickly and accurately with ML techniques. The same can be said for the segmentation of composites that contain multiple types of

materials, such as Li-ion battery electrodes, which encompass metal oxides, carbon particles and polymers. Such impressive segmentation capabilities allow electrochemically active and inactive materials, as well as pores, to be distinguished faster than ever before, triggering the emergence of the powerful digital twins of real electrode electrochemical operation. Still, the challenge remains for CT to distinguish polymeric binders from carbon additives, as both materials affect differently the overall electrode performance. ML is also expected to help accelerate the diagnostics of microstructural phenomena, as well as the identification of favourable particle and electrode architectures for a long life and for specific operating conditions.

Applying ML generative adversarial networks (GANs) to artificially create representative electrode microstructures[12] holds promise for generating 3D-resolved images with greater detail than any single imaging mode could achieve. GANs, trained with CT volumes or even slices[151], can also be used to generate in silico extended volumes. This would be particularly suitable for developing representative electrochemistry simulations from pre-existing tomography data of composite or electrode structures. The combination of physical-based manufacturing models and GANs can also allow the quick generation of composite structures for compositions not yet characterized, which opens tremendous opportunities to accelerate the prediction and optimization of the impact of manufacturing conditions on the structures[119,152].

Critical to the acceleration of the adoption of ML techniques for these purposes is to make robust multiscale data open source, which would not only alleviate the limitation of accessing specialized imaging facilities but also provide a wealth of microstructural information available for ML and multiphysics and/or multiscale models. Such repositories should contain not only the actual data but also the metadata, which would allow us to precisely track the conditions in which the characterization was performed, and some initiatives have already emerged[153].

We also expect the emergence of AI- and ML-orchestrated workflows that integrate CT characterization, data analysis and physical model generation at multiple scales (multiscale modelling) (Fig. 5)[73]. By coupling existing middleware technologies (for example, UNICORE, https://www.unicore.eu) to AI and ML scripts, such workflows may not be difficult to develop. Thus, ML can be used to sequentially or iteratively couple different length-scale models automatically with varying degrees of fidelity[154,155]. Moreover, ML can also assist in comparing the modelling outcomes with experimental data. The outputs can then later be used to train AI and ML models to predict the synthesis and manufacturing conditions needed to achieve the optimal material properties[156]. Such an automated high-fidelity approach may revolutionize the conception of new composite materials by linking experimental data (CT) with computational simulations.

Conclusions

Since its conception in the 1970s, CT has profoundly impacted the scientific community. In the past two decades, it has extended to greatly influence battery research and development. As a non-destructive tool, CT can perform powerful in situ and operando studies in a multitude of battery chemistries. The reconstructed volume and extracted morphological parameters (for example, particle size distribution, porosity and tortuosity) can be incorporated in predictive models to simulate battery performances. Using AI and ML techniques, such as GANs, CT images can also be used to generate large representative volumes of multiphase porous electrode microstructures[12]. The advent of such techniques can drastically reduce the number of required CT characterizations for 3D-resolved electrochemical models and also ensure representative volumes for simulations.

Additionally, the combination of multiscale 3D morphological characterization techniques (for example, FIB–SEM, TEM, micro-CT and nano-CT) may pave the way for performance-predictive models that can incorporate phenomena at multiple length scales. Characterization data and models can then be consolidated in open-source datasets and repositories, and even incorporated in virtual-reality environments and tools to educate a new generation of researchers on electrode structures and associated geometric features[157]. With the tremendous progresses achieved in these past 20 years in CT experimentation, analysis and computational modelling, and in AI and ML, there is the promise of remarkable achievements and discoveries in the years to come.

References

1. Seeram, E. Computed tomography: a technical review. *Radiol. Technol.* **89**, 279CT–302CT (2018).
2. Pietsch, P. & Wood, V. X-ray tomography for lithium ion battery research: a practical guide. *Annu. Rev. Mater. Res.* **47**, 451–479 (2017).
3. *Extend the Limits of Your Exploration: ZEISS Xradia 610 and 620 Versa* (ZEISS, accessed 10 December 2020); https://asset-downloads.zeiss.com/catalogs/download/mic/8fb6e06e-de4e-46dc-a9c9-883396ca1628/EN_product-information_610-620-Versa_rel1-3.pdf
4. Röntgen, W. C. On a new kind of rays. *Science* **3**, 227–231 (1896).
5. Knutsson, F. Röntgen and the Nobel Prize: with notes from his correspondence with Svante Arrhenius. *Acta Radiol. Diagn.* **8**, 449–460 (1969).
6. Radon, J. Über die Bestimmung von Funktionen durch ihre Integralwerte längs gewisser Mannigfaltigkeiten. *Akad. Wiss.* **69**, 262–277 (1917).
7. Rubin, G. D. Computed tomography: revolutionizing the practice of medicine for 40 years. *Radiology* **273**, S45–S74 (2014).
8. Christoph, R. & Neumann, H. J. *X-ray Tomography in Industrial Metrology: Precise, Economical and Universal* (Süddeutscher, 2011).
9. Villarraga-Gómez, H., Herazo, E. L. & Smith, S. T. X-ray computed tomography: from medical imaging to dimensional metrology. *Precis. Eng.* **60**, 544–569 (2019).
10. Heenan, T. M. M., Tan, C., Hack, J., Brett, D. J. L. & Shearing, P. R. Developments in X-ray tomography characterization for electrochemical devices. *Mater. Today* **31**, 69–85 (2019).
11. Zenyuk, I. V. Bridging X-ray computed tomography and computational modeling for electrochemical energy-conversion and -storage. *Curr. Opin. Electrochem.* **13**, 78–85 (2019).
12. Gayon-Lombardo, A., Mosser, L., Brandon, N. P. & Cooper, S. J. Pores for thought: generative adversarial networks for stochastic reconstruction of 3D multi-phase electrode microstructures with periodic boundaries. *npj Comput. Mater.* **6**, 82 (2020).
13. Petrich, L. et al. Crack detection in lithium-ion cells using machine learning. *Comput. Mater. Sci.* **136**, 297–305 (2017).
14. Jiang, Z. et al. Machine-learning-revealed statistics of the particle–carbon/binder detachment in lithium-ion battery cathodes. *Nat. Commun.* **11**, 2310 (2020).
15. Chiro, G. D. & Brooks, R. A. The 1979 Nobel Prize in Physiology or Medicine. *J. Comput. Assist. Tomogr.* **4**, 241–245 (1980).
16. Beckmann, E. C. CT scanning the early days. *Br. J. Radiol.* **79**, 5–8 (2006).
17. Hounsfield, G. N. Computerized transverse axial scanning (tomography): part 1. Description of system. *Br. J. Radiol.* **46**, 1016–1022 (1973).
18. Boerckel, J. D., Mason, D. E., McDermott, A. M. & Alsberg, E. Microcomputed tomography: approaches and applications in bioengineering. *Stem Cell Res. Ther.* **5**, 144 (2014).
19. Krüger, P. et al. Synchrotron X-ray tomography for investigations of water distribution in polymer electrolyte membrane fuel cells. *J. Power Sources* **196**, 5250–5255 (2011).
20. Fazeli, M. et al. Pore network modeling to explore the effects of compression on multiphase transport in polymer electrolyte membrane fuel cell gas diffusion layers. *J. Power Sources* **335**, 162–171 (2016).
21. Alrwashdeh, S. S. et al. In operando quantification of three-dimensional water distribution in nanoporous carbon-based layers in polymer electrolyte membrane fuel cells. *ACS Nano* **11**, 5944–5949 (2017).
22. Rawson, S. D., Maksimcuka, J., Withers, P. J. & Cartmell, S. H. X-ray computed tomography in life sciences. *BMC Biol.* **18**, 21 (2020).
23. Elliott, J. C. & Dover, S. D. X-ray microtomography. *J. Microsc.* **126**, 211–213 (1982).
24. Kress, J. W. & Feldkamp, L. A. "X-ray tomography applied to NDE of ceramics. In *Proc. ASME 1983 International Gas Turbine Conference and Exhibit. Volume 5: Ceramics; Structures and Dynamics; Controls, Diagnostics and Instrumentation; Education; Process Industries* V005T11A003 (American Society of Mechanical Engineers, 1983); https://doi.org/10.1115/83-GT-206

25. Stock, S. R. X-ray microtomography of materials. *Int. Mater. Rev.* **44**, 141–164 (1999).

26. Grodzins, L. Critical absorption tomography of small samples. *Nucl. Instrum. Methods Phys. Res.* **206**, 547–552 (1983).

27. Grodzins, L. Optimum energies for X-ray transmission tomography of small samples. *Nucl. Instrum. Methods Phys. Res.* **206**, 541–545 (1983).

28. Thompson, A. C. et al. Computed tomography using synchrotron radiation. *Nucl. Instrum. Methods Phys. Res.* **222**, 319–323 (1984).

29. Heiken, J. P., Brink, J. A. & Vannier, M. W. Spiral (helical) CT. *Radiology* **189**, 647–656 (1993).

30. Kalender, W. A., Seissler, W., Klotz, E. & Vock, P. in *Classic Papers in Modern Diagnostic Radiology* (eds Adrian, M. K. et al.) 1–68 (Springer, 2005).

31. Polacin, A., Kalender, W. A. & Marchal, G. Evaluation of section sensitivity profiles and image noise in spiral CT. *Radiology* **185**, 29–35 (1992).

32. Rubin, G. D., Leung, A. N., Robertson, V. J. & Stark, P. Thoracic spiral CT: influence of subsecond gantry rotation on image quality. *Radiology* **208**, 771–776 (1998).

33. Hu, H., He, H. D., Foley, W. D. & Fox, S. H. Four multidetector-row helical CT: image quality and volume coverage speed. *Radiology* **215**, 55–62 (2000).

34. Ballabriga, R. et al. Photon counting detectors for X-ray imaging with emphasis on CT. *IEEE Trans. Radiat. Plasma Med. Sci.* **5**, 422–440 (2021).

35. Kruth, J. P. et al. Computed tomography for dimensional metrology. *CIRP Ann.* **60**, 821–842 (2011).

36. Steinbock, L. & Dustmann, C.-H. Investigation of the inner structures of ZEBRA cells with a microtomograph. *J. Electrochem. Soc.* **148**, A132 (2001).

37. Sinha, P. K., Halleck, P. & Wang, C.-Y. Quantification of liquid water saturation in a PEM fuel cell diffusion medium using X-ray microtomography. *Electrochem. Solid State Lett.* **9**, A344 (2006).

38. Shearing, P. R., Howard, L. E., Jørgensen, P. S., Brandon, N. P. & Harris, S. J. Characterization of the 3-dimensional microstructure of a graphite negative electrode from a Li-ion battery. *Electrochem. Commun.* **12**, 374–377 (2010).

39. Hutzenlaub, T., Thiele, S., Zengerle, R. & Ziegler, C. Three-dimensional reconstruction of a LiCoO₂ Li-ion battery cathode. *Electrochem. Solid State Lett.* **15**, A33 (2011).

40. Yan, B., Lim, C., Yin, L. & Zhu, L. Three dimensional simulation of galvanostatic discharge of LiCoO₂ cathode based on X-ray nano-CT images. *J. Electrochem. Soc.* **159**, A1604 (2012).

41. Ebner, M., Marone, F., Stampanoni, M. & Wood, V. Visualization and quantification of electrochemical and mechanical degradation in Li ion batteries. *Science* **342**, 716–720 (2013).

42. Loveridge, M. et al. Looking deeper into the Galaxy (Note 7). *Batteries* **4**, 3 (2018).

43. Carter, R., Huhman, B., Love, C. T. & Zenyuk, I. V. X-ray computed tomography comparison of individual and parallel assembled commercial lithium iron phosphate batteries at end of life after high rate cycling. *J. Power Sources* **381**, 46–55 (2018).

44. Maire, E. & Withers, P. J. Quantitative X-ray tomography. *Int. Mater. Rev.* **59**, 1–43 (2014).

45. Gelb, J., Finegan, D. P., Brett, D. J. L. & Shearing, P. R. Multi-scale 3D investigations of a commercial 18650 Li-ion battery with correlative electron- and X-ray microscopy. *J. Power Sources* **357**, 77–86 (2017).

46. Finegan, D. P. et al. Investigating lithium-ion battery materials during overcharge-induced thermal runaway: an operando and multi-scale X-ray CT study. *Phys. Chem. Chem. Phys.* **18**, 30912–30919 (2016).

47. Gelb, J. et al. Energy tunability in laboratory 3D nano-XRM. *Microsc. Microanal.* **25**, 388–389 (2019).

48. *2022 NSLS-II Strategic Plan* (Brookhaven National Laboratory, 2021).

49. Chenevier, D. & Joly, A. ESRF: inside the extremely brilliant source upgrade. *Synchrotron Radiat. News* **31**, 32–35 (2018).

50. Rack, A. Hard X-ray imaging at ESRF: exploiting contrast and coherence with the new EBS storage ring. *Synchrotron Radiat. News* **33**, 20–28 (2020).

51. Meirer, F. et al. Three-dimensional imaging of chemical phase transformations at the nanoscale with full-field transmission X-ray microscopy. *J. Synchrotron Radiat.* **18**, 773–781 (2011).

52. Müller, S. et al. Multimodal nanoscale tomographic imaging for battery electrodes. *Adv. Energy Mater.* **10**, 1904119 (2020).

53. Falch, K. V. et al. Zernike phase contrast in high-energy X-ray transmission microscopy based on refractive optics. *Ultramicroscopy* **184**, 267–273 (2018).

54. Withers, P. J. X-ray nanotomography. *Mater. Today* **10**, 26–34 (2007).

55. Yin, L. et al. High performance printed AgO–Zn rechargeable battery for flexible electronics. *Joule* **5**, 228–248 (2021).

56. Pietsch, P. et al. Quantifying microstructural dynamics and electrochemical activity of graphite and silicon–graphite lithium ion battery anodes. *Nat. Commun.* **7**, 12909 (2016).

57. Taiwo, O. O. et al. Microstructural degradation of silicon electrodes during lithiation observed via operando X-ray tomographic imaging. *J. Power Sources* **342**, 904–912 (2017).

58. Gonzalez, J. et al. Three dimensional studies of particle failure in silicon based composite electrodes for lithium ion batteries. *J. Power Sources* **269**, 334–343 (2014).

59. Vanpeene, V. et al. Dynamics of the morphological degradation of Si-based anodes for Li-ion batteries characterized by in situ synchrotron X-ray tomography. *Adv. Energy Mater.* **9**, 1803947 (2019).

60. Gent, W. E. et al. Persistent state-of-charge heterogeneity in relaxed, partially charged Li₁₋ₓNi₁/₃Co₁/₃Mn₁/₃O₂ secondary particles. *Adv. Mater.* **28**, 6631–6638 (2016).

61. Holzner, C. et al. Zernike phase contrast in scanning microscopy with X-rays. *Nat. Phys.* **6**, 883–887 (2010).

62. Komini Babu, S., Mohamed, A. I., Whitacre, J. F. & Litster, S. Multiple imaging mode X-ray computed tomography for distinguishing active and inactive phases in lithium-ion battery cathodes. *J. Power Sources* **283**, 314–319 (2015).

63. Chen-Wiegart, Y. K., Liu, Z., Faber, K. T., Barnett, S. A. & Wang, J. 3D analysis of a LiCoO₂–Li(Ni₁/₃Mn₁/₃Co₁/₃)O₂ Li-ion battery positive electrode using X-ray nano-tomography. *Electrochem. Commun.* **28**, 127–130 (2013).

64. Heenan, T. M. M. et al. Resolving Li-ion battery electrode particles using rapid lab-based X-ray nano-computed tomography for high-throughput quantification. *Adv. Sci.* **7**, 2000362 (2020).

65. Frisco, S., Kumar, A., Whitacre, J. F. & Litster, S. Understanding Li-ion battery anode degradation and pore morphological changes through nano-resolution X-ray computed tomography. *J. Electrochem. Soc.* **163**, A2636–A2640 (2016).

66. Su, Z. et al. X-ray nanocomputed tomography in Zernike phase contrast for studying 3D morphology of Li–O₂ battery electrode. *ACS Appl. Energy Mater.* **3**, 4093–4102 (2020).

67. Ngandjong, A. C. et al. Investigating electrode calendering and its impact on electrochemical performance by means of a new discrete element method model: towards a digital twin of Li-Ion battery manufacturing. *J. Power Sources* **485**, 229320 (2021).

68. Torayev, A. et al. Stochasticity of pores interconnectivity in Li–O₂ batteries and its impact on the variations in electrochemical performance. *J. Phys. Chem. Lett.* **9**, 791–797 (2018).

69. Torayev, A., Magusin, P. C. M. M., Grey, C. P., Merlet, C. & Franco, A. A. Importance of incorporating explicit 3D-resolved electrode mesostructures in Li–O₂ battery models. *ACS Appl. Energy Mater.* **1**, 6433–6441 (2018).

70. Ding, N. et al. Influence of carbon pore size on the discharge capacity of Li–O₂ batteries. *J. Mater. Chem. A* **2**, 12433–12441 (2014).

71. Epstein, N. On tortuosity and the tortuosity factor for flow and diffusion through porous media. *Chem. Eng. Sci.* **44**, 777–779 (1989).

72. Tjaden, B., Brett, D. J. L. & Shearing, P. R. Tortuosity in electrochemical devices: a review of calculation approaches. *Int. Mater. Rev.* **63**, 47–67 (2018).

73. Lu, X. et al. 3D microstructure design of lithium-ion battery electrodes assisted by X-ray nano-computed tomography and modelling. *Nat. Commun.* **11**, 2079 (2020).

74. Usseglio-Viretta, F. L. E. et al. Quantitative relationships between pore tortuosity, pore topology, and solid particle morphology using a novel discrete particle size algorithm. *J. Electrochem. Soc.* **167**, 100513 (2020).

75. Ebner, M., Chung, D.-W., García, R. E. & Wood, V. Tortuosity anisotropy in lithium-ion battery electrodes. *Adv. Energy Mater.* **4**, 1301278 (2014).

76. *Submicron X-ray Imaging: Maintain High Resolution Even at Large Working Distances: ZEISS Xradia Versa 510* (ZEISS, accessed 27 September 2020); https://asset-downloads.zeiss.com/catalogs/download/mic/59f564ec-a757-4f23-9607-b4ae6d91c05e/EN_product-info_Xradia-510-Versa_rel-1.2.pdf

77. Varslot, T., Kingston, A., Myers, G. & Sheppard, A. High-resolution helical cone-beam micro-CT with theoretically-exact reconstruction from experimental data. *Med. Phys.* **38**, 5459–5476 (2011).

78. Li, T. et al. Three-dimensional reconstruction and analysis of all-solid Li-ion battery electrode using synchrotron transmission X-ray microscopy tomography. *ACS Appl. Mater. Interfaces* **10**, 16927–16931 (2018).

79. Ghorbani Kashkooli, A. et al. Synchrotron X-ray nano computed tomography based simulation of stress evolution in LiMn₂O₄ electrodes. *Electrochim. Acta* **247**, 1103–1116 (2017).

80. *ZEISS Xradia 810 Ultra—Nanoscale X-ray Imaging: Explore at the Speed of Science* (ZEISS, accessed 10 December 2020); https://asset-downloads.zeiss.com/catalogs/download/mic/c5e5bd17-4f66-42df-a4b3-18ecd933024e/EN_product-info_Xradia-810-Ultra_rel3.0.pdf

81. Frisco, S. et al. Internal morphologies of cycled Li-metal electrodes investigated by nano-scale resolution X-ray computed tomography. *ACS Appl. Mater. Interfaces* **9**, 18748–18757 (2017).

82. Yermukhambetova, A. et al. Exploring 3D microstructural evolution in Li–sulfur battery electrodes using in-situ X-ray tomography. *Sci. Rep.* **6**, 35291 (2016).

83. Yufit, V. et al. Investigation of lithium-ion polymer battery cell failure using X-ray computed tomography. *Electrochem. Commun.* **13**, 608–610 (2011).

84. Taiwo, O. O. et al. Investigating the evolving microstructure of lithium metal electrodes in 3D using X-ray computed tomography. *Phys. Chem. Chem. Phys.* **19**, 22111–22120 (2017).

85. Ito, Y., Wei, X., Desai, D., Steingart, D. & Banerjee, S. An indicator of zinc morphology transition in flowing alkaline electrolyte. *J. Power Sources* **211**, 119–128 (2012).

86. Ko, J. S. et al. Robust 3D Zn sponges enable high-power, energy-dense alkaline batteries. *ACS Appl. Energy Mater.* **2**, 212–216 (2019).

87. Mitsch, T. et al. Preparation and characterization of Li-ion graphite anodes using synchrotron tomography. *Materials* **7**, 4455–4472 (2014).

88. Arlt, T., Schröder, D., Krewer, U. & Manke, I. In operando monitoring of the state of charge and species distribution in zinc air batteries using X-ray tomography and model-based simulations. *Phys. Chem. Chem. Phys.* **16**, 22273–22280 (2014).

89. Yu, Y.-S. et al. Three-dimensional localization of nanoscale battery reactions using soft X-ray tomography. *Nat. Commun.* **9**, 921 (2018).

90. Tonin, G. et al. Operando investigation of the lithium/sulfur battery system by coupled X-ray absorption tomography and X-ray diffraction computed tomography. *J. Power Sources* **468**, 228287 (2020).

91. Lewis, J. A. et al. Linking void and interphase evolution to electrochemistry in solid-state batteries using operando X-ray tomography. *Nat. Mater.* **20**, 503–510 (2021).

92. Wang, J., Chen-Wiegart, Y. K. & Wang, J. In situ three-dimensional synchrotron X-ray nanotomography of the (de)lithiation processes in tin anodes. *Angew. Chem. Int. Ed.* **53**, 4460–4464 (2014).

93. Vanpeene, V. et al. Monitoring the morphological changes of Si-based electrodes by X-ray computed tomography: a 4D-multiscale approach. *Nano Energy* **74**, 104848 (2020).

94. Christensen, M. K., Mathiesen, J. K., Simonsen, S. B. & Norby, P. Transformation and migration in secondary zinc–air batteries studied by in situ synchrotron X-ray diffraction and X-ray tomography. *J. Mater. Chem. A* **7**, 6459–6466 (2019).

95. Choi, P., Parimalam, B. S., Su, L., Reeja-Jayan, B. & Litster, S. Operando particle-scale characterization of silicon anode degradation during cycling by ultrahigh-resolution X-ray microscopy and computed tomography. *ACS Appl. Energy Mater.* **4**, 1657–1665 (2021).

96. Jervis, R. et al. In situ compression and X-ray computed tomography of flow battery electrodes. *J. Energy Chem.* **27**, 1353–1361 (2018).

97. Doux, J. et al. Stack pressure considerations for room-temperature all-solid-state lithium metal batteries. *Adv. Energy Mater.* **10**, 1903253 (2020).

98. Franke-lang, R., Arlt, T., Manke, I. & Kowal, J. X-ray tomography as a powerful method for zinc–air battery research. *J. Power Sources* **370**, 45–51 (2017).

99. Tippens, J. et al. Visualizing chemomechanical degradation of a solid-state battery electrolyte. *ACS Energy Lett.* **4**, 1475–1483 (2019).

100. Scharf, J. et al. Investigating degradation modes in Zn–AgO aqueous batteries with in situ X-ray micro computed tomography. *Adv. Energy Mater.* https://doi.org/10.1002/aenm.202101327 (2021).

101. Lu, B. et al. Quantitatively designing porous copper current collectors for lithium metal anodes. *ACS Appl. Energy Mater.* **4**, 6454–6465 (2021).

102. Flannery, B. P., Deckman, H. W., Roberge, W. G. & D'amico, K. L. Three-dimensional X-ray microtomography. *Science* **237**, 1439–1444 (1987).

103. Daemi, S. R. et al. 4D visualisation of in situ nano-compression of Li-ion cathode materials to mimic early stage calendering. *Mater. Horiz.* **6**, 612–617 (2019).

104. Hubbell, J. H. & Seltzer, S. M. *Tables of X-Ray Mass Attenuation Coefficients and Mass Energy-Absorption Coefficients 1 keV to 20 meV for Elements Z = 1 to 92 and 48 Additional Substances of Dosimetric Interest* (NIST, accessed 18 February 2021); https://www.osti.gov/biblio/76335

105. Usseglio-Viretta, F. L. E. et al. Resolving the discrepancy in tortuosity factor estimation for Li-ion battery electrodes through micro–macro modeling and experiment. *J. Electrochem. Soc.* **165**, A3403–A3426 (2018).

106. Bailey, J. J. et al. Laser-preparation of geometrically optimised samples for X-ray nano-CT. *J. Microsc.* **267**, 384–396 (2017).

107. Tan, C. et al. Evolution of electrochemical cell designs for in-situ and operando 3D characterization. *Materials* **11**, 2157 (2018).

108. Ho, A. S. et al. 3D detection of lithiation and lithium plating in graphite anodes during fast charging. *ACS Nano* **15**, 10480–10487 (2021).

109. Nelson, J. et al. Identifying and managing radiation damage during in situ transmission X-ray microscopy of Li-ion batteries. *Proc. SPIE* **8851**, 88510B (2013).

110. Borkiewicz, O. J., Wiaderek, K. M., Chupas, P. J. & Chapman, K. W. Best practices for operando battery experiments: influences of X-ray experiment design on observed electrochemical reactivity. *J. Phys. Chem. Lett.* **6**, 2081–2085 (2015).

111. Kulkarni, D., Normile, S. J., Connolly, L. G. & Zenyuk, I. V. Development of low temperature fuel cell holders for operando X-ray micro and nano computed tomography to visualize water distribution. *J. Phys. Energy* **2**, 044005 (2020).

112. Finegan, D. P. et al. Spatial dynamics of lithiation and lithium plating during high-rate operation of graphite electrodes. *Energy Environ. Sci.* **13**, 2570–2584 (2020).

113. Pietsch, P., Hess, M., Ludwig, W., Eller, J. & Wood, V. Combining operando synchrotron X-ray tomographic microscopy and scanning X-ray diffraction to study lithium ion batteries. *Sci. Rep.* **6**, 27994 (2016).

114. Finegan, D. P. et al. Spatially resolving lithiation in silicon–graphite composite electrodes via in situ high-energy X-ray diffraction computed tomography. *Nano Lett.* **19**, 3811–3820 (2019).

115. Doyle, M., Fuller, T. F. & Newman, J. Modeling of galvanostatic charge and discharge of the lithium/polymer/insertion cell. *J. Electrochem. Soc.* **140**, 1526–1533 (1993).

116. Newman, J. S. & Tobias, C. W. Theoretical analysis of current distribution in porous electrodes. *J. Electrochem. Soc.* **109**, 1183 (1962).

117. Landesfeind, J., Ebner, M., Eldiven, A., Wood, V. & Gasteiger, H. A. Tortuosity of battery electrodes: validation of impedance-derived values and critical comparison with 3D tomography. *J. Electrochem. Soc.* **165**, A469–A476 (2018).

118. Trembacki, B. L. et al. Editors' choice—mesoscale analysis of conductive binder domain morphology in lithium-ion battery electrodes. *J. Electrochem. Soc.* **165**, E725–E736 (2018).

119. Duquesnoy, M., Lombardo, T., Chouchane, M., Primo, E. N. & Franco, A. A. Data-driven assessment of electrode calendering process by combining experimental results, in silico mesostructures generation and machine learning. *J. Power Sources* **480**, 229103 (2020).

120. Chouchane, M., Rucci, A. & Franco, A. A. A versatile and efficient voxelization-based meshing algorithm of multiple phases. *ACS Omega* **4**, 11141–11144 (2019).

121. Cooper, S. J., Bertei, A., Shearing, P. R., Kilner, J. A. & Brandon, N. P. TauFactor: an open-source application for calculating tortuosity factors from tomographic data. *SoftwareX* **5**, 203–210 (2016).

122. Westhoff, D. et al. Parametric stochastic 3D model for the microstructure of anodes in lithium-ion power cells. *Comput. Mater. Sci.* **126**, 453–467 (2017).

123. Kashkooli, A. G. et al. Multiscale modeling of lithium-ion battery electrodes based on nano-scale X-ray computed tomography. *J. Power Sources* **307**, 496–509 (2016).

124. Yan, B., Lim, C., Yin, L. & Zhu, L. Simulation of heat generation in a reconstructed $LiCoO_2$ cathode during galvanostatic discharge. *Electrochim. Acta* **100**, 171–179 (2013).

125. Ngandjong, A. C. et al. Multiscale simulation platform linking lithium ion battery electrode fabrication process with performance at the cell level. *J. Phys. Chem. Lett.* **8**, 5966–5972 (2017).

126. Roberts, S. A., Brunini, V. E., Long, K. N. & Grillet, A. M. A framework for three-dimensional mesoscale modeling of anisotropic swelling and mechanical deformation in lithium-ion electrodes. *J. Electrochem. Soc.* **161**, F3052–F3059 (2014).

127. Ferraro, M. E., Trembacki, B. L., Brunini, V. E., Noble, D. R. & Roberts, S. A. Electrode mesoscale as a collection of particles: coupled electrochemical and mechanical analysis of NMC cathodes. *J. Electrochem. Soc.* **167**, 013543 (2020).

128. Chouchane, M., Primo, E. N. & Franco, A. A. Mesoscale effects in the extraction of the solid-state lithium diffusion coefficient values of battery active materials: physical insights from 3D modeling. *J. Phys. Chem. Lett.* **11**, 2775–2780 (2020).

129. Danner, T. et al. Thick electrodes for Li-ion batteries: a model based analysis. *J. Power Sources* **334**, 191–201 (2016).

130. Chouchane, M. & Franco, A. A. Deconvoluting the impacts of the active material skeleton and the inactive phase morphology on the performance of lithium ion battery electrodes. *Energy Storage Mater.* **47**, 649–655 (2022).

131. Lim, C., Yan, B., Yin, L. & Zhu, L. Simulation of diffusion-induced stress using reconstructed electrodes particle structures generated by micro/nano-CT. *Electrochim. Acta* **75**, 279–287 (2012).

132. Qiu, G. et al. 3-D pore-scale resolved model for coupled species/charge/fluid transport in a vanadium redox flow battery. *Electrochim. Acta* **64**, 46–64 (2012).

133. Zhang, D. et al. The effect of wetting area in carbon paper electrode on the performance of vanadium redox flow batteries: a three-dimensional lattice Boltzmann study. *Electrochim. Acta* **283**, 1806–1819 (2018).

134. Wang, M. et al. Numerical evaluation of the effect of mesopore microstructure for carbon electrode in flow battery. *J. Power Sources* **424**, 27–34 (2019).

135. Zhang, D. et al. Understanding the role of the porous electrode microstructure in redox flow battery performance using an experimentally validated 3D pore-scale lattice Boltzmann model. *J. Power Sources* **447**, 227249 (2020).

136. Harris, W. M. & Chiu, W. K. S. Determining the representative volume element size for three-dimensional microstructural material characterization. Part 1: predictive models. *J. Power Sources* **282**, 552–561 (2015).

137. Harris, W. M. & Chiu, W. K. S. Determining the representative volume element size for three-dimensional microstructural material characterization. Part 2: application to experimental data. *J. Power Sources* **282**, 622–629 (2015).

138. Roberts, S. A., Mendoza, H., Brunini, V. E. & Noble, D. R. A verified conformal decomposition finite element method for implicit, many-material geometries. *J. Comput. Phys.* **375**, 352–367 (2018).

139. Landstorfer, M., Prifling, B. & Schmidt, V. Mesh generation for periodic 3D microstructure models and computation of effective properties. *J. Comput. Phys.* **431**, 110071 (2021).

140. Chouchane, M. & Franco, A. A. An invitation to engage with computational modeling: user-friendly tool for in silico battery component generation and meshing. *Batter. Supercaps* **4**, 1451–1456 (2021).

141. Chouchane, M., Rucci, A., Lombardo, T., Ngandjong, A. C. & Franco, A. A. Lithium ion battery electrodes predicted from manufacturing simulations: Assessing the impact of the carbon-binder spatial location on the electrochemical performance. *J. Power Sources* **444**, 227285 (2019).

142. Lu, X. et al. Microstructural evolution of battery electrodes during calendering. *Joule* **4**, 2746–2768 (2020).

143. Lombardo, T. et al. Accelerated optimization methods for force-field parametrization in battery electrode manufacturing modeling. *Batteries Supercap.* **3**, 721–730 (2020).

144. Lombardo, T., Ngandjong, A. C., Belhcen, A. & Franco, A. A. Carbon-binder migration: a three-dimensional drying model for lithium-ion battery electrodes. *Energy Storage Mater.* **43**, 337–347 (2021).

145. Lombardo, T. et al. The ARTISTIC online calculator: exploring the impact of lithium-ion battery electrode manufacturing parameters interactively through your browser. *Batter. Supercaps* **5**, e202100324 (2022).

146. Burnett, T. L. et al. Correlative tomography. *Sci. Rep.* **4**, 4711 (2015).

147. Slater, T. J. et al. Multiscale correlative tomography: an investigation of creep cavitation in 316 stainless steel. *Sci. Adv.* **7**, 7332 (2017).

148. Apeleo Zubiri, B. et al. Correlative laboratory nano-CT and 360° electron tomography of macropore structures in hierarchical zeolites. *Adv. Mater. Interfaces* **8**, 2001154 (2021).

149. Daemi, S. R. et al. Visualizing the carbon binder phase of battery electrodes in three dimensions. *ACS Appl. Energy Mater.* **1**, 3702–3710 (2018).

150. Xu, H., Usseglio-Viretta, F., Kench, S., Cooper, S. J. & Finegan, D. P. Microstructure reconstruction of battery polymer separators by fusing 2D and 3D image data for transport property analysis. *J. Power Sources* **480**, 229101 (2020).

151. Kench, S. & Cooper, S. J. Generating three-dimensional structures from a two-dimensional slice with generative adversarial network-based dimensionality expansion. *Nat. Mach. Intell.* **3**, 299–305 (2021).

152. Franco, A. A. Escape from flatland. *Nat. Mach. Intell.* **3**, 277–278 (2021).

153. De Carlo, F. et al. TomoBank: a tomographic data repository for computational X-ray science. *Meas. Sci. Technol.* **29**, 034004 (2018).

154. Quinn, A. et al. Electron backscatter diffraction for investigating lithium-ion electrode particle architectures. *Cell Rep. Phys. Sci.* **1**, 100137 (2020).

155. Urban, A., Seo, D.-H. & Ceder, G. Computational understanding of Li-ion batteries. *npj Comput. Mater.* **2**, 16002 (2016).

156. Xu, H. et al. Guiding the design of heterogeneous electrode microstructures for Li-ion batteries: microscopic imaging, predictive modeling, and machine learning. *Adv. Energy Mater.* **11**, 2003908 (2021).

157. Franco, A. A. et al. Entering the augmented era: immersive and interactive virtual reality for battery education and research. *Batter. Supercaps* **3**, 1147–1164 (2020).

158. Andrade, V. D. et al. Fast X-ray nanotomography with sub-10 nm resolution as a powerful imaging tool for nanotechnology and energy storage applications. *Adv. Mater.* **33**, 2008653 (2021).

159. Oikonomou, C. M., Chang, Y.-W. & Jensen, G. J. A new view into prokaryotic cell biology from electron cryotomography. *Nat. Rev. Microbiol.* **14**, 205–220 (2016).

160. Lee, J. Z. et al. Cryogenic focused ion beam characterization of lithium metal anodes. *ACS Energy Lett.* **4**, 489–493 (2019).

161. Seidman, D. N. Three-dimensional atom-probe tomography: advances and applications. *Annu. Rev. Mater. Res.* **37**, 127–158 (2007).

162. Borgia, G. C., Camaiti, M., Cerri, F., Fantazzini, P. & Piacenti, F. Study of water penetration in rock materials by nuclear magnetic resonance tomography: hydrophobic treatment effects. *J. Cultural Herit.* **1**, 127–132 (2000).

163. Walther, F. et al. Visualization of the interfacial decomposition of composite cathodes in argyrodite-based all-solid-state batteries using time-of-flight secondary-ion mass spectrometry. *Chem. Mater.* **31**, 3745–3755 (2019).

164. Schlüter, S., Sheppard, A., Brown, K. & Wildenschild, D. Image processing of multiphase images obtained via X-ray microtomography: a review. *Water Resour. Res.* **50**, 3615–3639 (2014).

165. Carvalho, L. E., Sobieranski, A. C. & von Wangenheim, A. 3D segmentation algorithms for computerized tomographic imaging: a systematic literature review. *J. Digit. Imaging* **31**, 799–850 (2018).

166. Arganda-Carreras, I. et al. Trainable WEKA segmentation: a machine learning tool for microscopy pixel classification. *Bioinformatics* **33**, 2424–2426 (2017).

167. Satjaritanun, P. et al. Observation of preferential pathways for oxygen removal through porous transport layers of polymer electrolyte water electrolyzers. *iScience* **23**, 101783 (2020).

168. Serra, J. *Image Analysis and Mathematical Morphology* Vol. I (Academic Press, 1982).

169. Ghani, M. U. et al. Noise power characteristics of a micro-computed tomography system. *J. Comput. Assist. Tomogr.* **41**, 82–89 (2017).

170. Orhan, K. *Micro-Computed Tomography (Micro-CT) in Medicine and Engineering* (Springer International, 2020).

171. Barrett, J. F. & Keat, N. Artifacts in CT: recognition and avoidance. *RadioGraphics* **24**, 1679–1691 (2004).

172. Iassonov, P. & Tuller, M. Application of segmentation for correction of intensity bias in X-ray computed tomography images. *Vadose Zone J.* **9**, 187 (2010).

173. Tuller, M., Kulkarni, R. & Fink, W. in *Soil–Water–Root Processes: Advances in Tomography and Imaging* (eds Anderson, S. H. & Hopmans, J. W.) 157–182 (Soil Science Society of America, 2015).

174. Perona, P. & Malik, J. Scale-space and edge detection using anisotropic diffusion. *IEEE Trans. Pattern Anal. Mach. Intell.* **12**, 629–639 (1990).

175. Russ, J. C., Matey, J. R., Mallinckrodt, A. J. & McKay, S. The image processing handbook. *Microsc. Microanal.* **17**, 843 (2011).

176. Gonzalez, R. C., Woods, R. E. & Eddins, S. Image segmentation. *Digit. Image Process.* **2**, 331–390 (2002).

Acknowledgements

Competing interests

The authors declare no competing interests.

Additional information

Correspondence should be addressed to Jonathan Scharf, Jean-Marie Doux or Ying Shirley Meng.

Publisher's note Springer Nature remains neutral with regard to jurisdictional claims in published maps and institutional affiliations.